

Examining the magnetic geometry of magnetic flux rope: from the view of single-point analysis

Zhaojin Rong¹, Chi Zhang¹, Chao Shen², Lucy Klinger³, Jiawei Gao¹, James A. Slavin⁴, Yongcun Zhang⁵, Yong Wei⁶, and Weixing Wan⁷

¹Key Laboratory of Earth and Planetary Physics, Institute of Geology and Geophysics, Chinese Academy of Sciences

²Harbin Institute of Technology

³Beijing International Center for Mathematical Research, Peking University

⁴University of Michigan-Ann Arbor

⁵State Key Laboratory for Space Weather, National Space Science Center, Chinese Academy of Sciences

⁶Institute of Geology and Geophysics, Chinese Academy of Sciences

⁷Institute of Geology and Geophysics, Chinese Academy of Sciences

November 21, 2022

Abstract

With Magnetospheric Multiscale Mission (MMS) observation of a magnetic flux rope of ion scale in magnetopause, we apply the single-point method presented by Rong et al., [2013] to study the magnetic field structure of flux rope. The calculated geometric parameters, e.g. axis orientation, helical handedness, current density, curvature radius, and boundaries of flux rope show well consistency with those derived from the multi-point methods. Thus, the single-point method of Rong et al., [2013] is reliable for studying the interior field structure of magnetic flux rope and could be applied widely to single-point spacecraft missions that examine the dynamics of flux rope.

1 **Examining the magnetic geometry of magnetic flux rope: from the view of**
2 **single-point analysis**

3
4 Chi Zhang^{1,2}, Zhaojin Rong^{1,2,3}, Chao Shen⁴, Lucy Klinger⁵, Jiawei Gao^{1,2}, James A. Slavin⁶,
5 Yongcun Zhang⁷, Yong Wei^{1,2,3}, and Weixing Wan^{1,2,3}

6 ¹Key Laboratory of Earth and Planetary Physics, Institute of Geology and Geophysics, Chinese
7 Academy of Sciences, Beijing, China

8 ²College of Earth Science, University of Chinese Academy of Sciences, Beijing, China

9 ³Beijing National Observatory of Space Environment, Institute of Geology and Geophysics,
10 Chinese Academy of Sciences, Beijing, China

11 ⁴Harbin Institute of Technology, Shenzhen, China

12 ⁵Beijing International Center for Mathematical Research, Peking University, China

13 ⁶Department of Climate and Space Sciences and Engineering, University of Michigan, Ann Arbor,
14 MI, USA

15 ⁷State Key Laboratory of Space Weather, National Space Science Center, Chinese Academy of
16 Sciences, Beijing, China

17
18 Corresponding author: Zhaojin Rong (rongzhaojin@mail.iggcas.ac.cn)

19
20 **Key Points:**

- 21 • A magnetic flux rope of ion-scale observed by MMS is studied by multiple analysis
22 methods.
- 23 • We demonstrated that the flux rope's geometry can be reliably inferred by the single-point
24 method developed by Rong et al. [2013].
- 25 • The method of Rong et al., [2013] can be applied widely to studies of flux rope that use
26 single-point spacecraft missions.

27 **Abstract**

28 With Magnetospheric Multiscale Mission (MMS) observation of a magnetic flux rope of ion
29 scale in magnetopause, we apply the single-point method presented by Rong et al., [2013] to
30 study the magnetic field structure of flux rope. The calculated geometric parameters, e.g. axis
31 orientation, helical handedness, current density, curvature radius, and boundaries of flux rope
32 show well consistency with those derived from the multi-point methods. Thus, the single-point
33 method of Rong et al., [2013] is reliable for studying the interior field structure of magnetic flux
34 rope and could be applied widely to single-point spacecraft missions that examine the dynamics
35 of flux rope.

36 **Plain Language Summary**

37 Magnetic flux ropes, characterized as magnetic field lines that wrap and rotate around a
38 central axis, are observed ubiquitously in the space environment. Magnetic flux ropes are usually
39 seen as the products of magnetic reconnection that releases magnetic field energy explosively.
40 An accurate determination of the flux rope's geometric parameters (e.g. axis orientation, current
41 density, curvature radius, boundaries) is important for studying its geometry and exploring its
42 origin and evolution. In principle, these geometric parameters can be addressed and derived by a
43 four-point analysis of Cluster or MMS tetrahedron. However, most spacecraft missions are
44 single-point measurements, thus limiting the application of multi-point analysis. A single-point
45 method that infers the axis orientation of flux rope was recently developed by Rong et al. [2013].
46 Compared to multi-point analysis methods that study a flux rope case observed by MMS
47 tetrahedron, we show the method of Rong et al. [2013], apart from axis orientation, can
48 reasonably infer the current density, helical handedness, curvature radius, and boundaries of flux
49 rope. Thus, it seems worthwhile to apply widely this single-point method by Rong et al. [2013]

50 to single-point spacecraft missions for the purpose of examining the geometry and dynamics of
51 flux ropes.

52 **1 Introduction**

53 Magnetic flux rope (MFR), manifested as helical magnetic field lines wrapping around an
54 axis, has been observed ubiquitously in the space plasma environment, e.g. Earth's magnetotail
55 [e.g., Slavin et al., 2003a, 2003b; Zhang et al., 2007; Yang et al., 2014; Sun et al., 2019], Earth's
56 magnetopause [e.g., Russel and Elphic, 1979; Eastwood et al., 2016; Akhavan-Tafti et al., 2018],
57 Martian magnetotail [Hara et al., 2017], Venusian magnetotail [Zhang et al., 2012], Mercury's
58 magnetotail [e.g., Dibraccio et al., 2015; Zhao et al., 2019], and interplanetary space [e.g.,
59 Burlaga, 1988; Lepping et al., 1990]. MFR is generally considered as a product of magnetic
60 reconnection that releases magnetic field energy explosively [e.g., Eastwood et al., 2016; Hones,
61 1977; Schindler, 1974; Wang et al., 2015; Zhou et al., 2017].

62 Accurate estimation of the axis orientation of MFR is vital for determining the magnetic
63 geometry of MFR and exploring its origin and evolution. This issue could well be solved by the
64 multi-point analysis with the advent of multi-spacecraft missions, e.g. Cluster mission [Escoubet
65 et al., 2001] and Magnetospheric Multiscale mission (MMS) [Burch et al., 2015]. The
66 multi-point methods developed so far, such as Minimum Directional Derivative (MDD) [Shi et
67 al., 2005; Shi et al., 2019], Multiple Triangulation Analysis (MTA) [Zhou et al., 2006], and
68 Magnetic Rotation Analysis (MRA) [Shen et al., 2007] can derive the axis orientation by
69 analyzing the spatial gradient of the magnetic field. However, most current spacecraft missions,
70 such as Geotail [Nishida et al., 1994], do not have the unique tetrahedron configuration like
71 Cluster or MMS, and thus face a great challenge in inferring the axis orientation of MFR.

72 In the past, several popular single-point methods have attempted to infer the axis orientation.
73 (1) The minimum variance analysis based on magnetic field (BMVA) [Sonnerup and Scheible,
74 1998]. It was argued that BMVA can infer the axis orientation relying on the calculated
75 orthogonal eigen directions of magnetic field variation. However, the tests showed that the
76 inferred axis orientation critically depends on the spacecraft's crossing trajectory [Moldwin and
77 Hughes, 1991; Burlaga, 1988; Xiao et al., 2004; Rong et al., 2013]; (2) The fit of force-free
78 model [e.g. Lundquist, 1950; Lepping et al., 1990; Eastwood et al., 2016]. One cannot guarantee
79 that the detected real field structure of MFR always fits well with the force-free model.
80 Multi-point analysis of Cluster demonstrated that only the field structure around MFR's center is
81 close to the force-free field [e.g. Yang et al., 2014]; (3) The technique of Grad-Shafranov (GS)
82 reconstruction [Hau and Sonnerup, 1999; Hu and Sonnerup, 2002]. For the GS technique, MFR
83 is assumed to be in approximate magnetohydrostatic equilibrium, and a trial scheme is performed
84 repeatedly to search for the axis orientation, for which the curve for total transverse pressure
85 (plasma pressure plus magnetic pressure) versus the magnetic vector potential in the inbound
86 crossing should ideally be equal to that of the outbound crossing. This method may yield a
87 reasonable solution of axis orientation, but at the expense of a trial scheme.

88 Recently, based on an assumption of azimuthal symmetry of MFR's helical field, Rong et
89 al., [2013] presented a simple single-point method (we refer to it as R13) to derive the axis
90 orientation of MFR. Application to the same MFR cases by the four spacecraft of Cluster
91 demonstrated that this method could infer the axis orientation consistently without restriction of
92 force-free field configuration. Nonetheless, the typical separation scale of Cluster tetrahedron is
93 about several hundred kilometers to thousands of kilometers, which is comparable to or larger
94 than the typical scale of MFR observed in magnetosphere. The multi-point analysis of Cluster on

95 the field structure of MFR could yield significant truncation error owing to the large separation
96 scale [e.g. Shen et al., 2003, 2007]. Therefore, Rong et al. [2013] did not make the direct
97 comparison between R13 and the multi-point analysis of Cluster.

98 The closely separated four spacecraft (separation scale 10~20 km) of MMS tetrahedron
99 [Burch et al., 2015], with unprecedented temporal and spatial resolutions measurements of
100 magnetic field and plasma, make it possible to evaluate the validity of R13 by comparison with
101 the multi-point analysis. The high-resolution of magnetic field is measured by a fluxgate
102 magnetometer operating at 128 vectors per second in burst-mode [Russell et al., 2014]. While
103 FPI (Fast Plasma Investigation) onboard MMS can measure the electrons at a burst cadence of
104 30ms and ions at a burst cadence of 150 ms, with an energy/charge range from 10 eV/q to 30000
105 eV/q. [Pollock et al., 2016]. The plasma moments are derived from the all-sky electron and ion
106 distributions by FPI.

107 As a continuation of Rong et al., [2013], by comparison with multi-point analysis methods
108 in analyzing a flux rope case observed by MMS tetrahedron, we show that R13, in addition to
109 axis orientation, is able to infer the consistent current density, helical handedness, curvature
110 radius, and boundaries of flux rope.

111 This paper is organized as follows: the method of R13 is briefly reviewed in Section 2; the
112 overview of studied MFR cases by MMS and the associated multi-point analysis results are
113 offered in Section 3; using R13, the axis orientation, current density, helical handedness,
114 curvature radius of magnetic field lines, and transverse boundaries of MFR are calculated and
115 identified in Section 4; and the conclusion and discussion are finally given in Section 5.

116

117 2. Review of R13

118 Rong et al., [2013] presented a single-point method based on the sampled magnetic field
 119 data by spacecraft to infer the axis orientation of MFR. This method makes two key assumptions
 120 are made in this method: (1) the relative trajectory of spacecraft crossing the MFR is straight; (2)
 121 the magnetic field structure of MFR is stable and can be seen as an ideal structure of azimuthal
 122 symmetry. The assumptions are usually acceptable, particularly for the innermost part of MFR
 123 where the field structure is the least affected by the interaction with ambient plasma. The
 124 available data are the relative velocity of spacecraft to cross MFR, \mathbf{V} , and the sampled magnetic
 125 field vector, \mathbf{B} , by spacecraft. The unit vector of relative velocity and magnetic field are $\hat{\mathbf{v}}$ ($\hat{\mathbf{v}}$
 126 $=\mathbf{V}/|\mathbf{V}|$) and $\hat{\mathbf{b}}$ ($\hat{\mathbf{b}}=\mathbf{B}/|\mathbf{B}|$) respectively.

127 The first step in applying this method is to seek out the innermost location where the
 128 spacecraft, along its trajectory, is closest to the center of MFR. In the cross-section of MFR,
 129 Figure 1a shows that \mathbf{v}_{\perp} and \mathbf{b}_{\perp} , the components of $\hat{\mathbf{v}}$ and $\hat{\mathbf{b}}$ perpendicular to the axis
 130 orientation respectively, would become parallel or antiparallel at the innermost location, and
 131 $\mathbf{v}_{\perp} \cdot \mathbf{b}_{\perp}$ would reach the extreme. Hence, by checking the time series of $\hat{\mathbf{v}} \cdot \hat{\mathbf{b}}$, the data point of
 132 innermost location could be identified. The identification of the innermost location is a key step
 133 in determining the axis orientation, because the axis orientation $\hat{\mathbf{n}}$, the unit field direction at the
 134 innermost time $\hat{\mathbf{b}}_{\text{in}}$, and $\hat{\mathbf{v}}$ should be coplanar (see Figure 1b).

135 The second step is to find the axis orientation $\hat{\mathbf{n}}$ in the plane formed by $\hat{\mathbf{b}}_{\text{in}}$ and $\hat{\mathbf{v}}$.
 136 Using the derived $\hat{\mathbf{b}}_{\text{in}}$, one can construct an orthogonal coordinate system $\{\hat{\mathbf{e}}_1, \hat{\mathbf{v}}, \hat{\mathbf{n}}_0\}$ to seek
 137 $\hat{\mathbf{n}}$ (see Figure 1b), where

138

$$\begin{aligned}\hat{\mathbf{e}}_1 &= \hat{\mathbf{v}} \times \hat{\mathbf{b}} / |\hat{\mathbf{v}} \times \hat{\mathbf{b}}| \\ \hat{\mathbf{n}}_0 &= \hat{\mathbf{e}}_1 \times \hat{\mathbf{v}}\end{aligned}\quad (1)$$

139 In the plane constituted by $\hat{\mathbf{b}}_{\text{in}}$ and $\hat{\mathbf{v}}$, the unsolved axis orientation $\hat{\mathbf{n}}$ deviates from $\hat{\mathbf{n}}_0$ by
 140 an angle of ψ . In other words, $\hat{\mathbf{n}}$ is a function of ψ . To constrain ψ , the evaluated impact
 141 distance r_0 (the closest distance of MFR's center to spacecraft trajectory) for each data point
 142 should be constant along the trajectory. The solved ψ or the optimal $\hat{\mathbf{n}}$ should result in a
 143 constant series of r_0 . Thus, Rong et al., [2013] constructed a residue error as a function of ψ ,

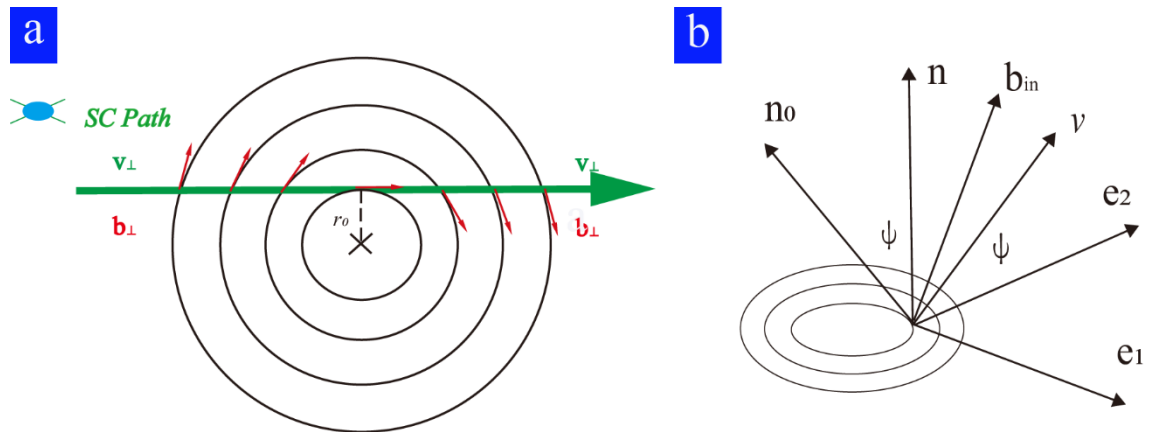
$$\sigma^2 = \frac{1}{M} \sum_i^M (r_{0i} - \langle r_0 \rangle)^2 \quad (2)$$

145 where, M is the number of data points and $\langle r_0 \rangle = \frac{1}{M} \sum_i^M (r_{0i})$. The axis orientation $\hat{\mathbf{n}}$ can be
 146 numerically solved when σ^2 reaches a minimum.

147 Here, to nondimensionalize the residue error, we suggest modifying Eq. (2) as

$$\sigma^2 = \frac{1}{M} \sum_i^M \left(1 - \frac{r_{0i}}{\langle r_0 \rangle}\right)^2 \quad (3)$$

149



150

151

152 **Figure 1:** Two schematic views of MFR. Panel a shows the variation of unit magnetic field
 153 direction along the trajectory of the spacecraft on the cross-section plane. The green arrow
 154 denotes the trajectory of the spacecraft, or can be regarded as the direction of \mathbf{v}_\perp . The red
 155 arrows represent the direction of \mathbf{b}_\perp . r_0 , as the impact distance, which is the closest distance
 156 to the center of the flux rope. Panel b shows the geometric relationship between $\{\hat{\mathbf{e}}_1, \hat{\mathbf{v}}, \hat{\mathbf{n}}_0\}$ and
 157 $\{\hat{\mathbf{e}}_1, \hat{\mathbf{e}}_2, \hat{\mathbf{n}}\}$.

158

159 With the optimal $\hat{\mathbf{n}}$ derived from Eq.(3), one can set up an orthogonal coordinate system
 160 $\{\hat{\mathbf{e}}_1, \hat{\mathbf{e}}_2, \hat{\mathbf{n}}\}$, and associated cylindrical coordinates $\{\hat{\mathbf{r}}, \hat{\phi}, \hat{\mathbf{n}}\}$ to describe the intrinsic helical field
 161 structure of MFR, where $\hat{\mathbf{e}}_2 = \hat{\mathbf{n}} \times \hat{\mathbf{e}}_1$ (see Figure 1b), $\hat{\mathbf{r}}$ is the unit radial vector from the
 162 center of MFR, and $\hat{\phi}$ is the unit azimuthal vector. In the cylindrical coordinates, the axial and
 163 azimuthal components of current density can be calculated respectively based on

$$164 \quad j_n = \mu_0^{-1} r^{-1} \frac{\partial(rB_\phi)}{\partial r}, j_\phi = -\mu_0^{-1} \frac{\partial B_n}{\partial r} \quad (4)$$

165 where μ_0 is the vacuum permeability coefficient, r is the radial distance to MFR's center, B_n
 166 and B_ϕ are the axial and azimuthal components of magnetic field respectively.

167 In this case, the curvature of magnetic field line of MFR, known as $\rho_c = (\hat{\mathbf{b}} \cdot \nabla) \hat{\mathbf{b}}$, can be
 168 reduced to

$$169 \quad \rho_c = -\frac{b_\phi^2}{r} \hat{\mathbf{r}} \quad (5)$$

170 where b_ϕ is the azimuthal component of $\hat{\mathbf{b}}$. Thus, the geometrical field structure of MFR can
171 be also determined readily by cylindrical coordinates.

172

173 **3 Multi-point analysis of case**

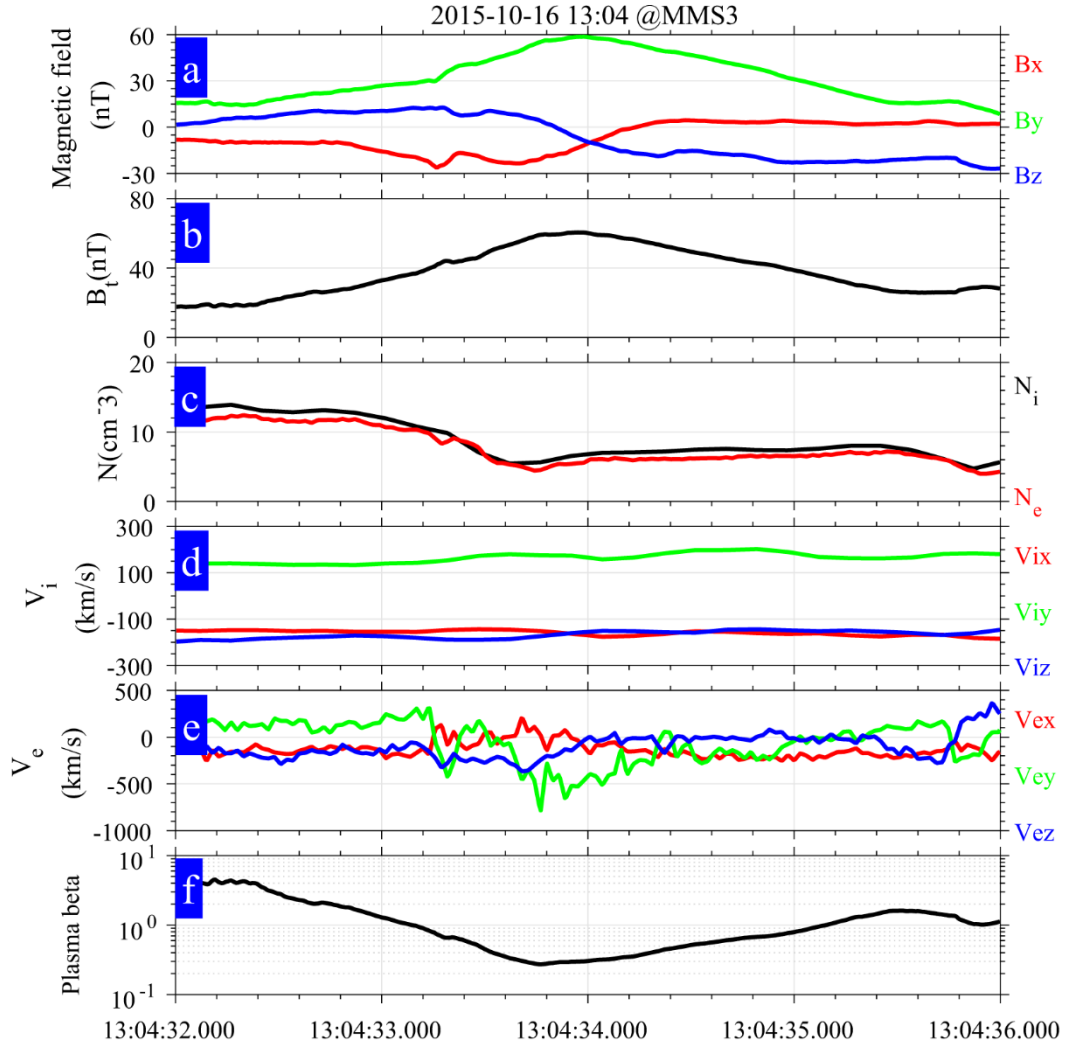
174 In this section, we apply R13 to study the magnetic structure of an MFR case observed by
175 MMS. Comparison with other methods, particularly with multi-point methods, highlights the
176 validity and plausibility of R13. The system utilized here is the Geocentric Solar Ecliptic (GSE)
177 coordinates unless otherwise stated.

178 **3.1 Overview of case**

179 Figure 2 shows an MFR case of ion-scale observed by MMS during 13:04:32-13:04:36 on
180 16 October 2015. MMS was located at $[X=8.33, Y=8.51, Z=-0.7]$ R_E , around the dayside
181 magnetopause during this period, and the separation scale of the tetrahedron was about 20 km.
182 This case, known as flux transfer events (FTEs) around magnetopause, has been studied by many
183 researchers [Eastwood et al., 2016; Zhao et al., 2016; Akhavan-Tafti et al., 2018].

184 The detected magnetic field data in Figure 2a shows bipolar signatures (-/+) for both B_x and
185 B_z components accompanied by enhanced magnetic field strength and ion flow of $-V_z$ direction.
186 These typical field signatures of MFR suggest that MMS3 may encounter a southward-moving
187 MFR. The ion and electron number density evidence a slight tendency to decrease towards
188 MFR's center, from $\sim 14\text{cm}^{-3}$ to 5cm^{-3} , and the plasma beta (the ratio of plasma pressure to
189 magnetic pressure) reaches a minimum around the center of MFR. The signatures of both
190 magnetic field and plasma are consistent with those reported in previous studies of MFR [e.g.
191 Slavin et al., 2003a; Akhavan-Tafti et al., 2018; Sun et al., 2019].

192



193

194 **Figure 2:** The flux rope case observed by MMS3 on 16 Oct. 2015. From up to bottom, the panels
 195 show the time series of magnetic field components in GSE, the field strength, the number density
 196 of ion and electron, the bulk velocity of ions and electrons in GSE, and the value of plasma beta.

197

198 3.2 Multi-Point Analysis

199 Previous studies suggested that the scale of MFR is about several hundred kilometers
 200 [Eastwood et al., 2016; Akhavan-Tafti et al., 2018], which is larger than the scale of MMS
 201 tetrahedron (~20 km). Thus, the magnetic field within tetrahedron could be better approximated

202 by linear-varied field, which favors the application of multi-point analysis methods to examine
 203 the geometric structure of a magnetic field, e.g. axis orientation, current density, curvature radius
 204 of magnetic field, etc. The parameters of field structure yielded could be treated as a benchmark
 205 for checking the validity of R13.

206 In this subsection, two popular multi-point analysis methods, i.e. MDD (Minimum
 207 Directional Derivative) and MRA (Magnetic Rotation Analysis), are used independently to infer
 208 the axis orientation.

209 MDD can determine the dimensionality of magnetic structure and has been successfully
 210 applied to analyzing the structure of flux rope [Shi et al., 2005; Shi et al., 2019; Sun et al., 2019].

211 The key step is to decompose the symmetrical matrix $(\nabla\mathbf{B})(\nabla\mathbf{B})^T$, where $\nabla\mathbf{B}$ is the gradient

212 tensor of magnetic field. Three eigenvalues $(\lambda_{\max}, \lambda_{\text{int}}, \lambda_{\min})$ and the corresponding

213 eigenvectors $(\hat{\mathbf{n}}_{\max}, \hat{\mathbf{n}}_{\text{int}}, \hat{\mathbf{n}}_{\min})$ can be obtained by decomposing $(\nabla\mathbf{B})(\nabla\mathbf{B})^T$. The

214 dimensionality of magnetic structure can be indicated by the three eigenvalues. If magnetic

215 structure is 1-D, we would have $\sqrt{\lambda_{\max}} \gg \sqrt{\lambda_{\text{int}}} \cong \sqrt{\lambda_{\min}}$, it would be

216 $\sqrt{\lambda_{\max}} \cong \sqrt{\lambda_{\text{int}}} \gg \sqrt{\lambda_{\min}}$ if it is 2-D.

217 Applying MDD to this case (see Figure 3a), we find $\sqrt{\lambda_{\max}} \sim 0.35$, $\sqrt{\lambda_{\text{int}}} \sim 0.25$, and

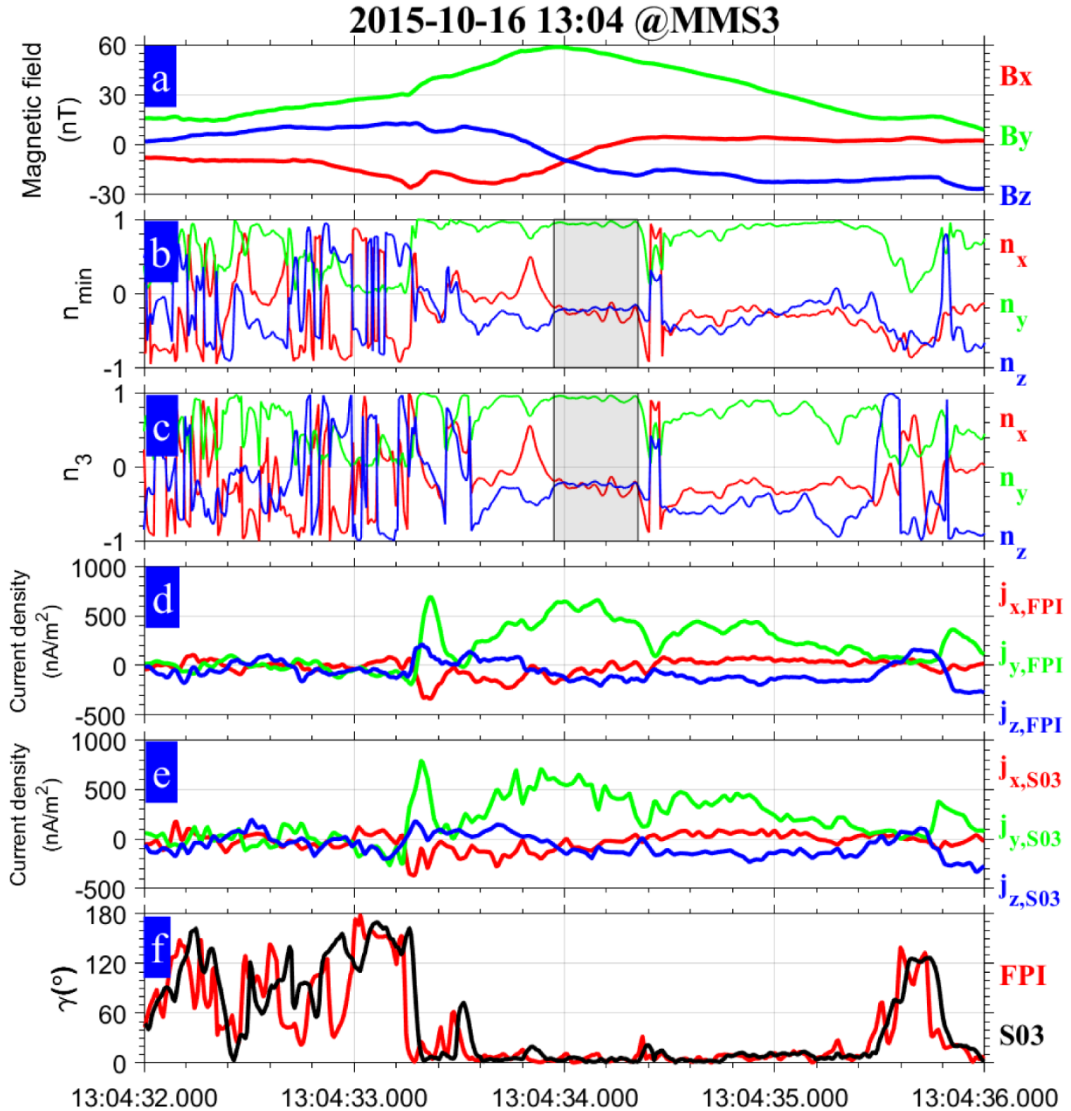
218 $\sqrt{\lambda_{\min}} \sim 0.03$ around the peak of magnetic field. Thus, the MFR is a 2-D structure, and the axis

219 orientation is along $\hat{\mathbf{n}}_{\min}$ [Shi et al., 2005; Shi et al., 2019]. We select an appropriate time

220 interval when $\hat{\mathbf{n}}_{\min}$ is stable around the peak of magnetic field (see the shaded interval

221 ‘13:04:33.950-13:04:34.350’ in Figure 3b). The mean of $\hat{\mathbf{n}}_{\min}$ within this interval demonstrates

222 that the axis orientation is $(-0.2618, 0.9416, -0.2119)$.



223

224 **Figure 3:** Multi-point analysis of a flux rope. From top to bottom, panels show: (a) magnetic225 field; (b) the eigenvector corresponding to λ_{\min} in MDD; (c) the eigenvector corresponding to226 μ_3 in MRA; (d) the current density derived by multi-point analysis of magnetic field; (e) current

227 density derived by plasma moments from FPI of MMS3; (f) the angle between current density

228 and the direction of magnetic field.

229

230 In contrast to MDD, MRA is performed to analyze the spatial rotation rates of magnetic
 231 field direction by decomposing the magnetic rotation tensor $(\nabla\hat{\mathbf{b}})(\nabla\hat{\mathbf{b}})^T$ [Shen et al., 2007].
 232 The decomposition of this tensor leads to three eigenvalues (μ_1, μ_2, μ_3) and three eigenvectors
 233 $(\hat{\mathbf{n}}_1, \hat{\mathbf{n}}_2, \hat{\mathbf{n}}_3)$. $\hat{\mathbf{n}}_1$, $\hat{\mathbf{n}}_2$, and $\hat{\mathbf{n}}_3$ represent the fastest, moderate, and slowest directions,
 234 respectively, along which the direction of magnetic field varies. Thus, $\hat{\mathbf{n}}_3$ is usually seen as the
 235 axis orientation of MFR when it was surveyed [Shen et al., 2007; Yang et al., 2014]. The time
 236 series of calculated $\hat{\mathbf{n}}_3$ is displayed in Figure 3c. With the same shaded interval in Figure 3b,
 237 the average axis orientation derived by MRA is $(-0.2679, 0.9338, -0.2373)$, which is nearly equal
 238 to that obtained by MDD. The inferred axis orientations from MDD and MRA are tabulated in
 239 Table 1.

240 According to $\mathbf{j} = \mu_0^{-1} \nabla \times \mathbf{B}$, the current density can be also solved based on a multi-point
 241 analysis that uses Taylor expansion by Shen et al., [2003] (it is referred to as S03). The
 242 calculated current density is shown in Figure 3d. Alternatively, with plasma moments measured
 243 by FPI onboard MMS3, Figure 3e shows the current density calculated by $\mathbf{j} = \mathbf{n}_e \mathbf{e}(\mathbf{V}_i - \mathbf{V}_e)$,
 244 where \mathbf{n}_e is the number density of electron, while \mathbf{V}_i and \mathbf{V}_e are the bulk velocity of
 245 protons and electrons respectively. Apparently, the two methods to calculate the current density
 246 shows much agreement, demonstrating that measurement of plasma moments by FPI can be
 247 employed to calculate the current density, and that the electron could be the main current carrier
 248 of MFR (not shown here).

249 The angle between current density and magnetic field, denoted as γ , is nearly equal to 0°
 250 in the center and trail of MFR (see Figure 3f), which indicates that the current density is basically

251 field-aligned, and suggests that the field structures at MFR's center and trail are close to the
 252 force-free field with a right-hand helical handedness [Eastwood et al., 2016].

253 **4. Application of R13**

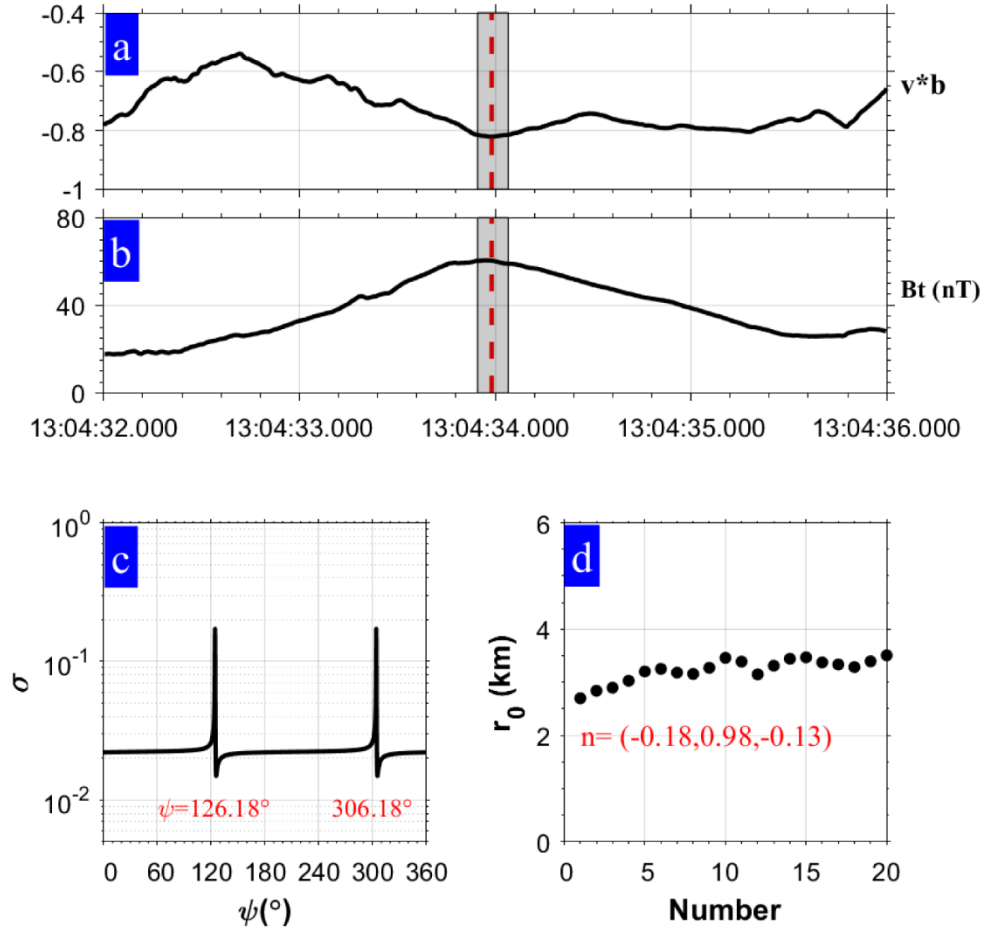
254 **4.1 Axis Orientation**

255
 256 We now perform R13 to analyze the field structure of this flux rope. Without loss of
 257 generality, we arbitrarily choose the data provided by MMS3 for our analysis.

258 Following the procedures of Rong et al., [2013], we identify the innermost time first by
 259 checking the time series of $\hat{\mathbf{v}} \cdot \hat{\mathbf{b}}$. With the assumption of crossing a quasi-stationary magnetic
 260 structure, the velocity of MFR can be seen as \mathbf{V}_{HT} , the velocity of DeHoffmann-Teller (HT)
 261 frame [Khrabrov and Sonnerup, 1998]. Thus, with HT analysis within interval 13:04:32-13:04:36,
 262 the relative velocity of spacecraft to MFR is calculated as $\mathbf{V} = -\mathbf{V}_{\text{HT}} = (167.88, -208.83, 165.94)$
 263 km/s. The correlation coefficient ~ 0.998 between $-\mathbf{V}_{\text{HT}} \times \mathbf{B}$ and $-\mathbf{V} \times \mathbf{B}$ (\mathbf{V} is the bulk ion
 264 velocity from FPI) guarantees the reliability of HT analysis. As a result, the unit vector of $\hat{\mathbf{v}}$ is
 265 derived as $\hat{\mathbf{v}} = \frac{\mathbf{V}}{|\mathbf{V}|} = (0.5327, -0.6626, 0.5265)$.

266 Figure 4a shows the time series of $\hat{\mathbf{v}} \cdot \hat{\mathbf{b}}$. Clearly, the product of $\hat{\mathbf{v}} \cdot \hat{\mathbf{b}}$ reaches a minimum
 267 around the peak of field strength (Figure 4b). Thus, corresponding to the minimum of $\hat{\mathbf{v}} \cdot \hat{\mathbf{b}}$, the
 268 time when the spacecraft is located at the innermost part or is closest to the MFR's center can be
 269 identified at 13:04:33.982 (see the red dashed lines in Figure 4a and Figure 4b). Accordingly,
 270 having identified the innermost time, the inferred $\hat{\mathbf{e}}_1$ is $(-0.7295, -0.0442, 0.6825)$, $\hat{\mathbf{n}}_0$ is
 271 $(0.4290, 0.7477, 0.5069)$, and the local coordinate system $\{\hat{\mathbf{e}}_1, \hat{\mathbf{v}}, \hat{\mathbf{n}}_0\}$ can be constructed via Eq.
 272 (1).

273 We choose a short interval centered at the innermost time with 20 sampled magnetic field
274 vectors to infer the axis orientation (a longer interval may contain the samples nearby the
275 boundary where field structures are significantly distorted). It should be noted that, as suggested
276 by Rong et al. [2013], the sampled data point at the innermost time has been excluded to avoid
277 the ill-calculation. By numerical calculation, we find that the residue error σ , defined in Eq. (3),
278 would reach a minimum ($\sigma_{\min}=0.015$) when the angle between $\hat{\mathbf{n}}$ and $\hat{\mathbf{n}}_0$, equals either
279 126.18° or 306.18° (Figure 4c), which results in a pair of anti-parallel axis-orientations in
280 principle. Following Rong et al., [2013], we choose the one pointing roughly along $\hat{\mathbf{b}}_{\text{in}}$ as the
281 final axis orientation. As a result, the axis orientation $\hat{\mathbf{n}}$ is derived as $(-0.1767, 0.9762, -0.1257)$,
282 and $\hat{\mathbf{e}}_2$ is estimated as $(0.6607, 0.2123, 0.7200)$. In other words, projected along the derived $\hat{\mathbf{n}}$,
283 the orientations of the 20 magnetic vectors in trajectory can be fitted best with a circular-like
284 field structure. We find the mean impact distance of those 20 data points is about ~ 3.2 km (see
285 Figure 4d), which indicates that, in this case, MMS3 was almost crossing MFR's center.



286

287 **Figure 4:** Analysis of a flux rope based on the single-point method proposed by Rong et al.,

288 [2013]. Panel a and panel b show the time series of $\hat{\mathbf{v}} \cdot \hat{\mathbf{b}}$ and the magnetic field strength

289 respectively. The red dashed lines mark the time when $\hat{\mathbf{v}} \cdot \hat{\mathbf{b}}$ reaches a minimum. Panel c shows

290 the variation of σ against ψ . Panel d displays the evaluated impact distances for the 20 data

291 points of magnetic vectors.

292

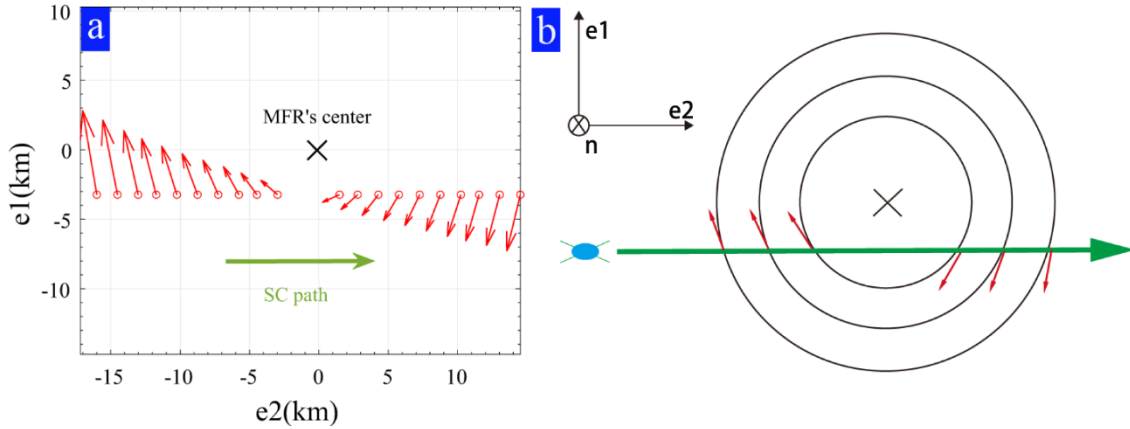
293 Since $\hat{\mathbf{e}}_1$, $\hat{\mathbf{e}}_2$ and $\hat{\mathbf{n}}$ are inferred, the orthogonal coordinate system $\{\hat{\mathbf{e}}_1, \hat{\mathbf{e}}_2, \hat{\mathbf{n}}\}$ is set up

294 to describe the intrinsic helical field structure of MFR. In this coordinate, Figure 5a shows the

295 projection of sampled \mathbf{b} (within the shaded interval) in the cross-section. Obviously, the

296 loop-like pattern of the projected field (also see Figure 5b) is consistent with the field-aligned
 297 current density near MFR center (see Figure 3c), which demonstrates the validity of R13.

298



299

300 **Figure 5:** (a) The projection of unit field vectors of sampled data points on the $\hat{e}_1 - \hat{e}_2$ plane.
 301 The red arrows represent the orientations of \mathbf{b}_\perp , and the green arrow represents the relative
 302 moving direction of the spacecraft crossing the MFR. The origin, marked as “x”, represents the
 303 MFR’s center. (b) A sketched diagram of the spacecraft crossing the MFR.

304

305 Repeating the same procedures as being conducted above, the axis orientations of this MFR
 306 based on the measurements of MMS1, MMS2, MMS4 are also inferred separately. The yielded
 307 results are tabulated in Table 1. As a comparison, the axis orientations by means of MDD and
 308 MRA, and fitting of force-free model [Eastwood et al., 2016], and a minimum variance analysis
 309 on gradient of magnetic pressure [Zhao et al., 2016] are also tabulated in Table1. In contrast to
 310 the single-point fitting method used by Eastwood et al. [2016], it seems the axis orientation
 311 inferred by R13 is closer to the axis orientation estimated by multi-point methods, i.e. MDD,
 312 MRA, and the analysis of magnetic pressure gradient by Zhao et al. [2016].

313

314 **Table 1:** The inferred axis-orientations by different methods.

SC ^a	$\hat{\mathbf{e}}_1$	$\hat{\mathbf{e}}_2$	$\hat{\mathbf{n}}$	Method ^b
MMS1	[-0.77, -0.10, 0.63]	[0.60, 0.22, 0.77]	[-0.21, 0.97, -0.11]	R13
MMS2	[-0.72, -0.02, 0.69]	[0.68, 0.17, 0.71]	[-0.14, 0.98, -0.11]	R13
MMS3	[-0.73, -0.04, 0.68]	[0.66, 0.21, 0.72]	[-0.18, 0.97, -0.13]	R13
MMS4	[-0.73, -0.05, 0.68]	[0.64, 0.30, 0.71]	[-0.24, 0.95, -0.19]	R13
All			[-0.24, 0.95, -0.22]	MDD
All			[-0.25, 0.94, -0.23]	MRA
MMS3			[-0.01, 0.99, -0.15]	E16
All			[-0.26, 0.90, -0.36]	Z16

315 ^a SC represents the spacecraft whose data is used.

316 ^b R13, E16, and Z16 represents, respectively, the single-point method presented by Rong et al.,
317 [2013], the fitting of force-free model by Eastwood et al., [2016], and the minimum variance
318 analysis on the gradient of magnetic pressure by Zhao et al., [2016].

319 **4.2 Current density and Curvature radius**

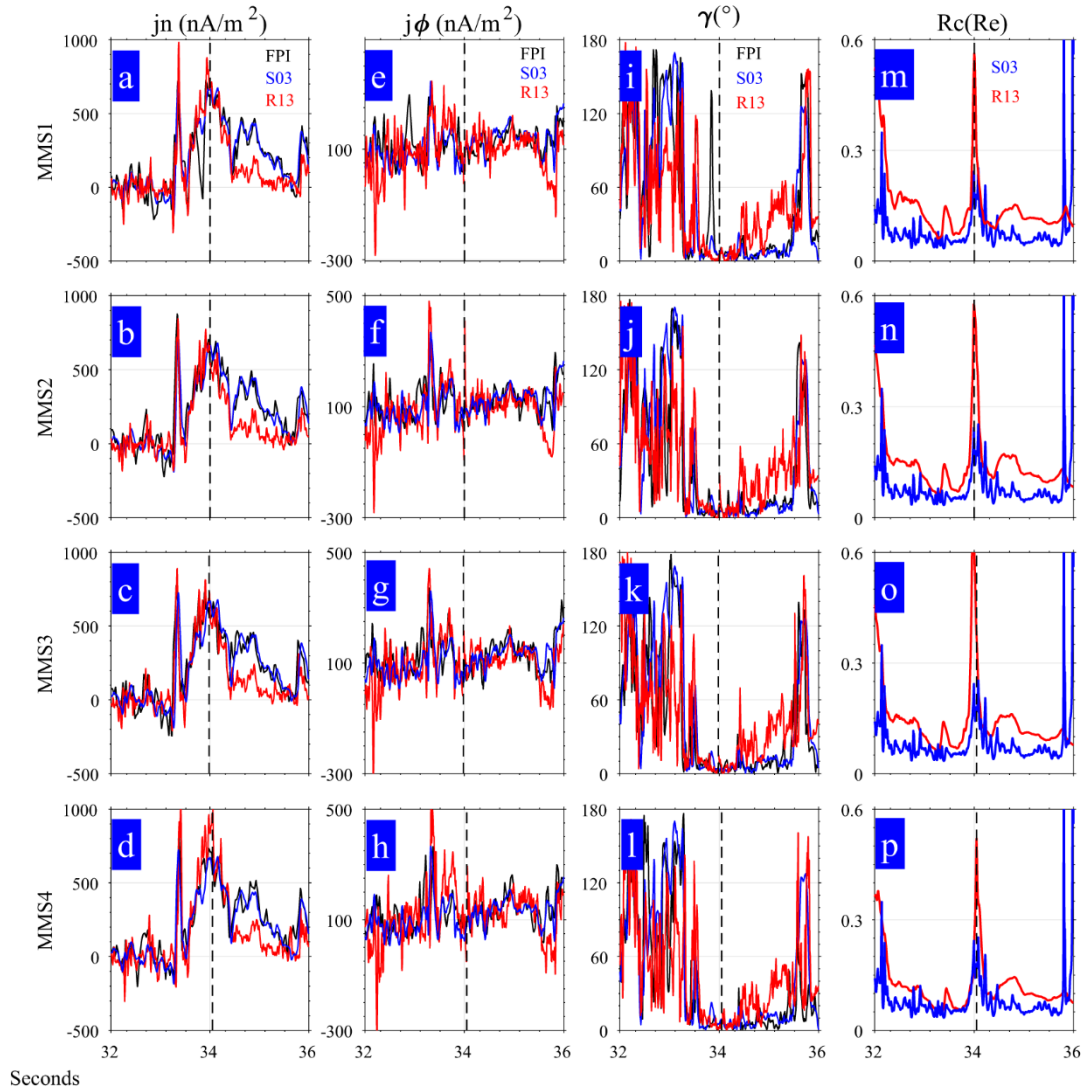
320 With the derived coordinate system $\{\hat{\mathbf{e}}_1, \hat{\mathbf{e}}_2, \hat{\mathbf{n}}\}$ for each spacecraft, we can examine the
321 current density and the curvature radius of magnetic field for associated cylindrical coordinates
322 $\{\hat{\mathbf{r}}, \hat{\phi}, \hat{\mathbf{n}}\}$ based on Eq. (4) and Eq. (5) respectively. The time series of calculated axial
323 component of current density, j_n , and the azimuthal component of current density, j_ϕ , for
324 MMS1, MMS2, MMS3, and MMS4 are shown in Figure 6a-6d and Figure 6e-6h, respectively.
325 The angle between current density and magnetic field, denoted as γ , is shown in Figure 6i-6l for
326 the four spacecraft.

327 In comparison to the current density calculated by $\mathbf{j} = n_e e (\mathbf{V}_i - \mathbf{V}_e)$ (black line) and
328 $\mathbf{j} = \mu_0^{-1} \nabla \times \mathbf{B}$ by S03 from (blue line), we find that the current density calculated by R13 for
329 each of the four spacecraft are consistent with that derived from the plasma moments and the curl
330 of magnetic field. From this latter current density, we notice a significant field-aligned current in
331 the MFR center and a filament peak of current ahead of it, suggesting that the magnetic field is

332 nearly force-free around the center but non-force-free in the outer or the draping region [Zhao et
333 al., 2016]. The consistent pattern of current density demonstrates that the method of R13 can
334 recover the distribution of current density of MFR (red line) by means of a one-point analysis.

335 The curvature radius of magnetic field is calculated separately for each of the four
336 spacecraft via Eq. (5), as shown in Figure 6m-6p. For comparison, the curvature radius
337 calculated by S03 is displayed. It is clear that the curvature radius from S03 is larger in MFR's
338 center ($\sim 0.25 R_E$) than in the outer region ($\sim 0.05 R_E$), which implies that magnetic field lines
339 become straighter in the MFR's center. This is consistent with previous studies [e.g., Slavin et al.,
340 2003; Shen et al., 2007; Yang et al., 2014]. It is interesting to note that R13 obtains the similar
341 pattern of curvature radius variation, but slightly overestimates the curvature radius. Because
342 R13 ignores axial and azimuthal components and only estimates the radial component of
343 curvature, the real curvature is underestimated and curvature radius is overestimated. The
344 discrepancy demonstrates that the actual field structure in the inner core of MFR cannot be an
345 ideal structure of azimuthal symmetry.

346



2015-10-16 13:04

347

348 **Figure 6:** The current density and curvature radius of MFR. The inferred axial components (j_n)
 349 of current density for four spacecraft are shown in panels a-d, the azimuthal components (j_ϕ) of
 350 current density are shown in panels e-h, and the angles between current density and local
 351 magnetic field direction are shown in panels i-l. The inferred curvature radiuses of magnetic
 352 field are shown in panels m-p. In these panels, the red and black lines represent the single-point
 353 results by R13 and plasma moment of FPI respectively. The blue lines represent the results of
 354 multi-point analysis by S03, which is the same for all panels in each column. The black dashed
 355 lines in all panels denote the time when the spacecraft is closest to the center of MFR.

4.3 Boundary or Size

With the derived axis orientation by R13, we could further study the helical field structure of MFR, and identify its boundaries or transverse size.

In the cross-section near the center of MFR (shown in Figure 7a), the projected magnetic field would be close to a circular configuration, and the displacement vector (\mathbf{r} , cyan lines) should be nearly perpendicular to the magnetic field vector (\mathbf{b}_\perp , red arrows). The angle α_{r,b_\perp} , defined as $\alpha_{r,b_\perp} = a \cos(|\mathbf{r} \cdot \mathbf{b}_\perp| / |\mathbf{r}| |\mathbf{b}_\perp|)$, is presumably close to 90° around the center of MFR. In contrast, in the outer part or boundary, α_{r,b_\perp} would deviate from 90° due to the distorted field structure induced by interaction with ambient plasma. Thus, the boundaries of MFR could be identified by checking the time series of α_{r,b_\perp} . The time series of α_{r,b_\perp} recorded by MMS3 is shown in Figure 7b. As expected, during the passage of MFR by spacecraft, α_{r,b_\perp} increases when the spacecraft moves towards MFR's center, stay about 90° when around the inner part, and finally decreases as it moves away from MFR.

Further, one can define a helical angle as $\theta = a \cos\left(\frac{B_\phi}{B_t}\right)$, where $B_\phi = |\mathbf{B} - (\mathbf{B} \cdot \hat{\mathbf{n}})\hat{\mathbf{n}}|$, to

study the helical geometry of MFR's field. Since the magnetic field in MFR's center is nearly parallel to the axis orientation, one would expect an increased helical angle when the distance to MFR's center is decreased. Figure 7c shows the calculated helical angle by R13 during the whole passage of MFR. For comparison, according to the axis orientation inferred from MRA, the helical angle from multi-point analysis is also displayed. The two methods yield an almost coincident time series of helical angle, suggesting the validity of the derived axis orientation by R13. In line with our expectations, we find the calculated helical angle increases as the

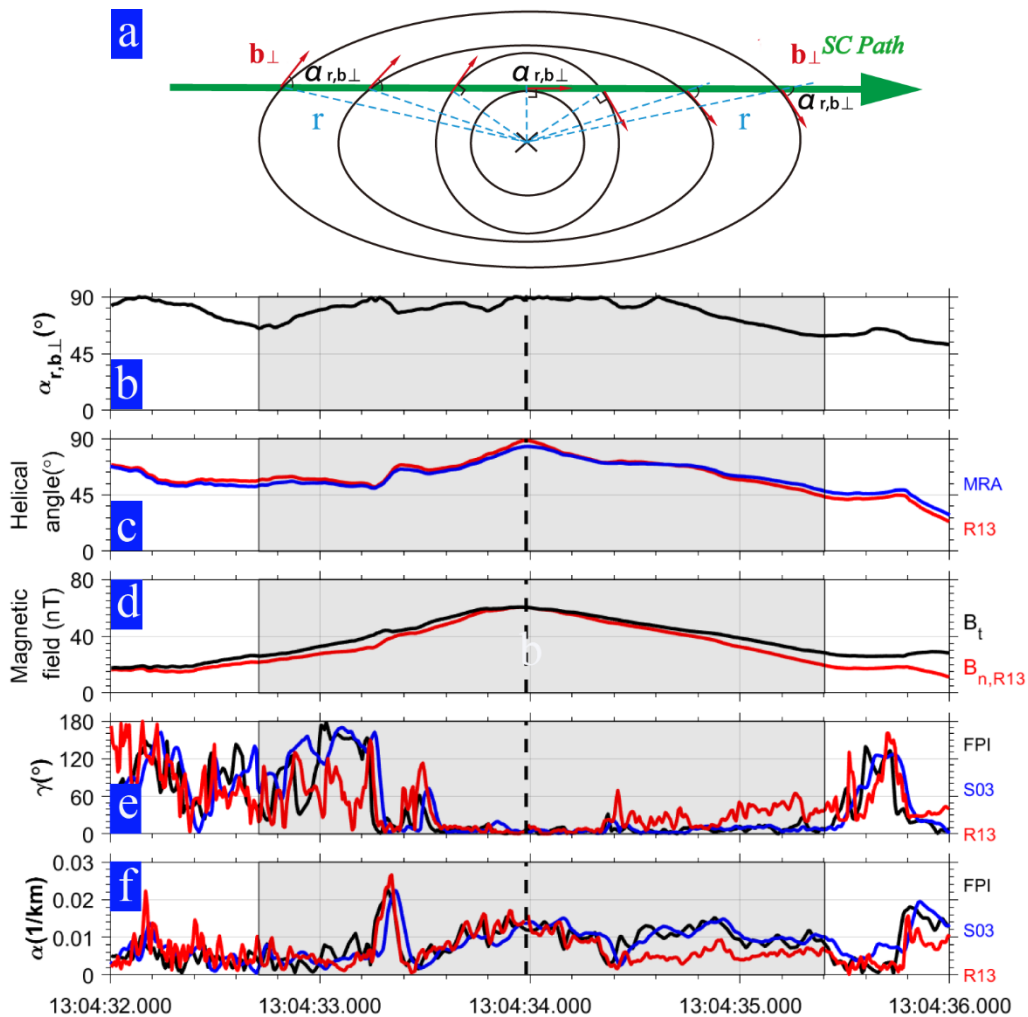
377 spacecraft approaches the innermost location, and decreases as it moves away from MFR. The
 378 maximum helical angle of nearly 90° demonstrates that the field lines around the innermost part
 379 are almost parallel to the axis orientation.

380 Therefore, considering the variation of α_{r,b_\perp} , the helical angle, and the axial component of
 381 magnetic field and field strength (Figure 7d), we suggest that the inbound and outbound crossing
 382 time of MFR boundaries should be 13:04:32.708 and 13:04:35.404, respectively. Thus, the
 383 interval of crossing the MFR is about 2.7 s (see the shaded interval in Figure 7b-7f). It is
 384 worthwhile to note that, with our identification of the boundaries, the frontal region or outer
 385 draping region with non-force-free field could be reasonably included within MFR (Figure 7e).

386 With the knowledge of axis orientation and the relative velocity of spacecraft ($\mathbf{V} = -\mathbf{V}_{HT}$),
 387 the transverse speed of crossing spacecraft is $|\mathbf{V}_\perp| = |\mathbf{V} - (\mathbf{V} \cdot \hat{\mathbf{n}})\hat{\mathbf{n}}| = 186$ km/s; thus the diameter
 388 (radius) of MFR is about 502 km (251 km). Interestingly, multi-point analysis by S03
 389 demonstrated that the curvature radius inside MFR is about $0.05 R_E$, or 319 km (see Figure
 390 6m-6p), which is comparable to the radius of MFR we estimated. In contrast, with the fit of
 391 force-free model, the radius of MFR estimated previously by Eastwood et al. [2016] and
 392 Akhavan-Tafti et al. [2018] is about 400~500 km, about twice of our estimation.

393 In the innermost part of this MFR, which has a low beta (~ 0.25) and a dominated
 394 field-aligned current (see Figure 2f and Figure 7e), the innermost field basically satisfies the
 395 force-free field [Lepping et al., 1990; Yang et al., 2014], $\nabla \times \mathbf{B} = \mu_0 \mathbf{j} = \alpha \mathbf{B}$. The calculated
 396 force-free factor α ($\alpha = \mu_0 j_t / B_t$) demonstrates that α is nearly constant (~ 0.013 km $^{-1}$) in
 397 the innermost of MFR, suggesting a linearly force-free field (Figure 7f).

398 Repeating the same procedures, the radius of MFR based on the measurements of MMS1,
 399 MMS2, MMS4 are also inferred separately. The results yielded are tabulated in Table 2.



400
 401 **Figure 7:** (a) A sketched diagram of flux rope; (b) the angle between the displacement vector
 402 and the direction of magnetic field (see definition in the text); (c) the helical angle; (d) the
 403 strength of magnetic field and the axial component of magnetic field derived from R13; (e) the
 404 angle between current density and orientation of magnetic field; (f) the force-free factor α . The
 405 black shaded interval represents the period of crossing the flux rope. The black dashed line
 406 denotes the time when the spacecraft is closest to the center of MFR.

407

408 **Table 2:** The inferred radius of MFR.

SC ^a	Interval ^b	V_{\perp} (km/s)	R(km) ^c	Method ^d
MMS1	13:04:32.808-13:04:35:590	186.42	259	R13
MMS2	13:04:32.736-13:04:35:572	199.95	284	R13
MMS3	13:04:32.708-13:04:35:404	186.06	251	R13
MMS4	13:04:32.784-13:04:35.409	155.58	204	R13
MMS3	~	~	550	E16
~	~	~	431	A18

409 ^a SC represents the spacecraft whose data is used. The symbol “~” means that the related
410 information is unclear.

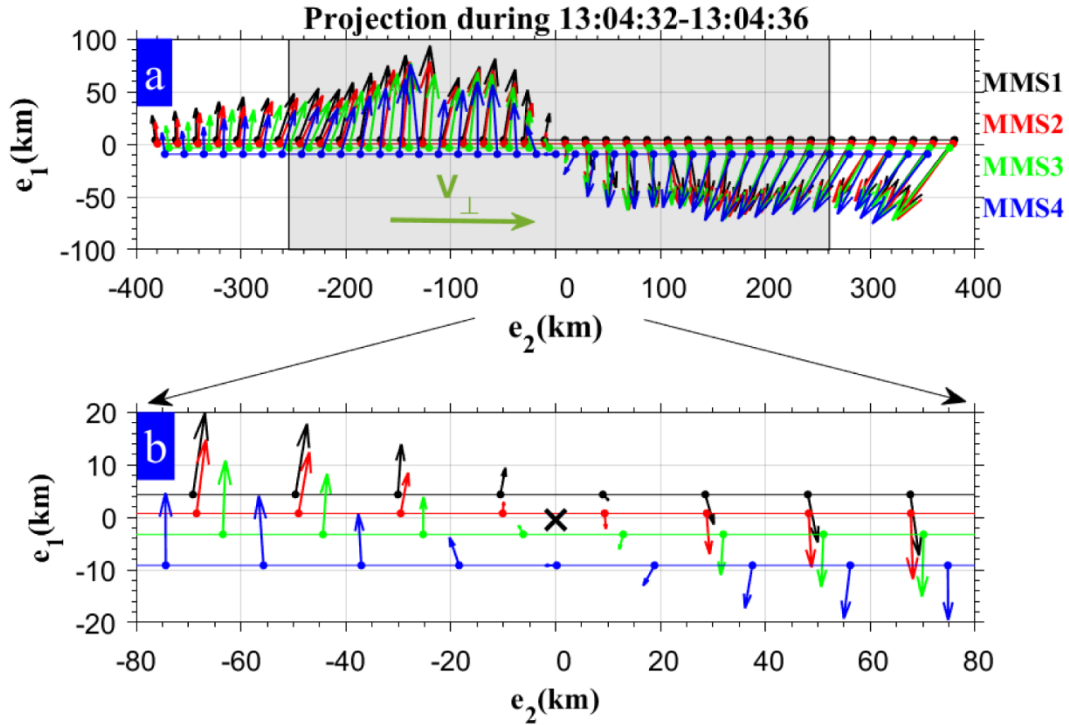
411 ^bThe duration of crossing MFR based on the variation of $\alpha_{r,b_{\perp}}$.

412 ^cThe radius of MFR.

413 ^dThe method applied in analyzing MFR. R13 and E16 are the same as defined in Table1. A18
414 represents the results based on the fit of force-free model by Akhavan-Tafti et al., [2018].

415

416 Using the inferred axis orientation and the transverse size of MFR based on the
417 measurements of MMS3, we project the field vectors recorded by four spacecraft on the
418 cross-section in Figure 8. The projected magnetic field near the MFR center is circular-like or
419 close to the structure of azimuthal symmetry (see Figure 8b), but is distorted or deviates from the
420 circular-like shape near the boundaries.



421

422 **Figure 8:** The projection of \mathbf{b}_\perp on the cross-section of flux rope. The resampled field vectors
 423 with a cadence of 0.1s as recorded by MMS1, MMS2, MMS3, MMS4 are labeled in black, red,
 424 green, and blue, respectively. The inferred size of MFR is shaded. Panel b zooms in on the
 425 projection of magnetic field vectors near the center of MFR.

426

427 4 Conclusion and Discussion

428 In this paper, by applying R13 to a magnetic flux rope observed by MMS tetrahedron in
 429 Earth's magnetopause, we analyze the magnetic field structure of magnetic flux rope. The
 430 parameters, including the axis orientation, the current density, the curvature radius of magnetic
 431 field, and the transverse size, are estimated by R13. With the estimated parameters, we conclude
 432 that: (1) the axis of MFR is basically orientated along the +Y-axis of GSE; (2) the field-aligned
 433 current is dominant in the interior of MFR where magnetic field is nearly force-free, and a
 434 filament peak of current is present in the leading part of MFR; (3) the helical handedness of

435 MFR is right-handed; (4) the curvature radius of magnetic field is larger in the MFR's center
436 than in the outer region ; (5) MFR's radius is about 250 km, suggesting the ion scale of MFR's
437 size.

438 The comparison with multi-point analysis methods demonstrates that R13 is reliable and
439 applicable. Therefore, the R13 can be applied widely to the "big dataset" accumulated by the
440 single-point spacecraft missions in history, e.g. Geotail, and to the planetary missions, e.g.
441 MAVEN [Jakosky et al., 2015], to study the geometry of flux rope and explore its origin,
442 evolution, and roles in the space environment.

443 We have to note that the key assumption of R13 is azimuthal symmetry of projected field
444 lines near the core of MFR. The assumption is more relaxed than that of the force-free model
445 which is employed to fit MFR in many previous studies [e.g. Burlaga, 1988; Lepping et al., 1990;
446 Slavin et al., 2003b]. However, the real field structure in the core of MFR absolutely cannot have
447 an ideal azimuthal symmetry as demonstrated by the non-zero minimum σ (Figure 4c) and the
448 overestimated curvature radius in MFR's center (Figure 6m-6p). Thus, the yielded parameters by
449 R13 must always be interpreted with caution.

450

451 **Acknowledgments**

452 The magnetic field data and plasma data of MMS used in this paper are available from the
453 MMS Science Data Center at <http://lasp.colorado.edu/mms/sdc/>. The authors are grateful to the
454 entire MMS team for providing the data. This work is supported by the Strategic Priority
455 Research Program of Chinese Academy of Sciences (Grant No. XDA17010201), the Key
456 Research Program of the Institute of Geology & Geophysics, CAS, Grant No. IGGCAS- 201904,
457 the National Natural Science Foundation of China (grants 41922031, 41774188, 41874190,

458 41874176, and 41621063) and NASA MMS Guest Investigator Grant 80NSSC18K1363. We
459 thank Nanqiao Du, Zhen Shi, Xinzou Li, Di Liu and Fang Qian for providing helpful
460 suggestions.

461

462 **References**

- 463 Akhavan-Tafti, M., Slavin, J. A., Le, G., Eastwood, J. P., Strangeway, R. J., Russell, C. T., ...
464 Burch, J. L. (2018). MMS Examination of FTEs at the Earth's Subsolar Magnetopause.
465 *Journal of Geophysical Research: Space Physics*, 123(2), 1224–1241.
466 <https://doi.org/10.1002/2017ja024681>.
- 467 Burch, J. L., Moore, T. E., Torbert, R. B., & Giles, B. L. (2015). Magnetospheric Multiscale
468 Overview and Science Objectives. *Space Science Reviews*, 199(1–4), 5–21.
469 <https://doi.org/10.1007/s11214-015-0164-9>.
- 470 Burlaga, L. F. (1988). Magnetic clouds and force-free fields with constant alpha. *Journal of*
471 *Geophysical Research*, 93(A7), 7217. <https://doi.org/10.1029/ja093ia07p07217>.
- 472 DiBraccio, G. A., Slavin, J. A., Imber, S. M., Gershman, D. J., Raines, J. M., Jackman, C. M., ...
473 Solomon, S. C. (2015). MESSENGER observations of flux ropes in Mercury's magnetotail.
474 *Planetary and Space Science*, 115, 77–89. <https://doi.org/10.1016/j.pss.2014.12.016>.
- 475 Eastwood, J. P., Phan, T. D., Cassak, P. A., Gershman, D. J., Haggerty, C., Malakit, K., ... Wang,
476 S. (2016). Ion-scale secondary flux ropes generated by magnetopause reconnection as
477 resolved by MMS. *Geophysical Research Letters*, 43(10), 4716–4724.
478 <https://doi.org/10.1002/2016gl068747>.
- 479 Elphic, R. C., & Russell, C. T. (1983). Magnetic flux ropes in the Venus ionosphere:
480 Observations and models. *Journal of Geophysical Research*, 88(A1), 58.
481 <https://doi.org/10.1029/ja088ia01p00058>.
- 482 Escoubet, C. P., Fehringer, M., & Goldstein, M. (2001). *Introduction* The Cluster mission.
483 *Annales Geophysicae*, 19(10/12), 1197–1200. <https://doi.org/10.5194/angeo-19-1197-2001>.
- 484 Hara, T., Harada, Y., Mitchell, D. L., DiBraccio, G. A., Espley, J. R., Brain, D. A., ... Jakosky,
485 B. M. (2017). On the origins of magnetic flux ropes in near-Mars magnetotail current sheets.
486 *Geophysical Research Letters*, 44(15), 7653–7662. <https://doi.org/10.1002/2017gl073754>.
- 487 Hau, L.-N., & Sonnerup, B. U. Ö. (1999). Two-dimensional coherent structures in the
488 magnetopause: Recovery of static equilibria from single-spacecraft data. *Journal of*
489 *Geophysical Research: Space Physics*, 104(A4), 6899–6917.
490 <https://doi.org/10.1029/1999ja900002>.
- 491 Hones, E. W., Jr. (1977). Substorm processes in the magnetotail: Comments on “On hot tenuous
492 plasmas, fireballs, and boundary layers in the Earth's magnetotail” by L. A. Frank, K. L.
493 Ackerson, and R. P. Lepping. *Journal of Geophysical Research*, 82(35), 5633–5640.
494 <https://doi.org/10.1029/ja082i035p05633>.
- 495 Hu, Q., & Sonnerup, B. U. Ö. (2002). Reconstruction of magnetic clouds in the solar wind:
496 Orientations and configurations. *Journal of Geophysical Research*, 107(A7), 1142.
497 <https://doi.org/10.1029/2001JA000293>.

- 498 Jakosky, B. M., Lin, R. P., Grebowsky, J. M., Luhmann, J. G., Mitchell, D. F., Beutelschies, G.,
499 Priser, T., Acuna, M., Andersson, L., Baird, D., Baker, D., Bartlett, R., Benna, M., Bougher,
500 S., Brain, D., Carson, D., Cauffman, S., Chamberlin, P., Chaufray, J.-Y., ... Zurek, R.
501 (2015). The Mars Atmosphere and Volatile Evolution (MAVEN) Mission. *Space Science*
502 *Reviews*, 195(1–4), 3–48. <https://doi.org/10.1007/s11214-015-0139-x>.
- 503 Khrabrov, A. V., and B. U. O. Sonnerup (1998), DeHoffmann-Teller analysis, in Analysis
504 Methods for Multi-Spacecraft Data, *ISSI Sci. Rep. SR- 001*, edited by G. Paschmann and P.
505 W. Daly, p. 221, Springer, New York.
- 506 Lepping, R. P., Jones, J. A., & Burlaga, L. F. (1990). Magnetic field structure of interplanetary
507 magnetic clouds at 1 AU. *Journal of Geophysical Research*, 95(A8), 11957.
508 <https://doi.org/10.1029/ja095ia08p11957>.
- 509 Lundquist, S. (1950), Magneto-hydrostatic fields. *Ark. Fys.*, 2, 316 – 365.
- 510 Moldwin, M. B., & Hughes, W. J. (1991). Plasmoids as magnetic flux ropes. *Journal of*
511 *Geophysical Research: Space Physics*, 96(A8), 14051–14064.
512 <https://doi.org/10.1029/91ja01167>.
- 513 Nishida, A. (1994). The Geotail Mission. *Geophysical Research Letters*, 21(25), 2871–2873.
514 <https://doi.org/10.1029/94gl01223>.
- 515 Pollock, C., Moore, T., Jacques, A., Burch, J., Gliese, U., Saito, Y., ... Zeuch, M. (2016). Fast
516 Plasma Investigation for Magnetospheric Multiscale. *Space Science Reviews*, 199(1–4),
517 331–406. <https://doi.org/10.1007/s11214-016-0245-4>.
- 518 Rong, Z. J., Wan, W. X., Shen, C., Zhang, T. L., Lui, A. T. Y., Wang, Y., ... Zong, Q.-G. (2013).
519 Method for inferring the axis orientation of cylindrical magnetic flux rope based on
520 single-point measurement. *Journal of Geophysical Research: Space Physics*, 118(1), 271–
521 283. <https://doi.org/10.1029/2012ja018079>.
- 522 Russell, C. T., & Elphic, R. C. (1979). ISEE observations of flux transfer events at the dayside
523 magnetopause. *Geophysical Research Letters*, 6(1), 33–36.
524 <https://doi.org/10.1029/gl006i001p00033>.
- 525 Russell, C. T., Anderson, B. J., Baumjohann, W., Bromund, K. R., Dearborn, D., Fischer, D., et
526 al. (2016). The Magnetospheric Multiscale magnetometers. *Space Science Reviews*, 199(1–
527 4), 189–256. <https://doi.org/10.1007/s11214-014-0057-3>.
- 528 Schindler, K. (1974). A theory of the substorm mechanism. *Journal of Geophysical Research*,
529 79(19), 2803–2810. <https://doi.org/10.1029/ja079i019p02803>.
- 530 Shen, C., Li, X., Dunlop, M., Liu, Z. X., Balogh, A., Baker, D. N., Hapgood, M., & Wang, X.
531 (2003). Analyses on the geometrical structure of magnetic field in the current sheet based
532 on cluster measurements. *Journal of Geophysical Research: Space Physics*, 108(A5).
533 <https://doi.org/10.1029/2002ja00>.
- 534 Shen, C., Li, X., Dunlop, M., Shi, Q. Q., Liu, Z. X., Lucek, E., & Chen, Z. Q. (2007). Magnetic
535 field rotation analysis and the applications. *Journal of Geophysical Research: Space*
536 *Physics*, 112(A6). <https://doi.org/10.1029/2005ja011584>.
- 537 Shi, Q. Q., Shen, C., Pu, Z. Y., Dunlop, M. W., Zong, Q.-G., Zhang, H., ... Balogh, A. (2005).
538 Dimensional analysis of observed structures using multipoint magnetic field measurements:
539 Application to Cluster. *Geophysical Research Letters*, 32(12).
540 <https://doi.org/10.1029/2005gl022454>.
- 541 Shi, Q. Q., Tian, A. M., Bai, S. C., Hasegawa, H., Degeling, A. W., Pu, Z. Y., ... Liu, Z. Q.
542 (2019). Dimensionality, Coordinate System and Reference Frame for Analysis of In-Situ

- 543 Space Plasma and Field Data. *Space Science Reviews*, 215(4).
544 <https://doi.org/10.1007/s11214-019-0601-2>.
- 545 Slavin, J. A. (2003a). Geotail observations of magnetic flux ropes in the plasma sheet. *Journal of*
546 *Geophysical Research*, 108(A1). <https://doi.org/10.1029/2002ja009557>.
- 547 Slavin, J. A., Lepping, R. P., Gjerloev, J., Goldstein, M. L., Fairfield, D. H., Acuna, M. H., ...
548 Bosqued, J. M. (2003b). Cluster electric current density measurements within a magnetic
549 flux rope in the plasma sheet. *Geophysical Research Letters*, 30(7).
550 <https://doi.org/10.1029/2002gl016411>.
- 551 Sonnerup, B. U. Ö., and M. Scheible (1998), Minimum and maximum variance analysis, in
552 Analysis Methods for Multi-Spacecraft Data, *ISSI Sci. Rep. no. SR-001*, edited by G.
553 Paschmann and P. W. Daly, chap. 8, pp. 185–220, European Space Agency, Noordwijk,
554 Netherlands.
- 555 Sun, W. J., Slavin, J. A., Tian, A. M., Bai, S. C., Poh, G. K., Akhavan-Tafti, M., ... Burch, J. L.
556 (2019). MMS Study of the Structure of Ion-Scale Flux Ropes in the Earth's Cross-Tail
557 Current Sheet. *Geophysical Research Letters*, 46(12), 6168–6177.
558 <https://doi.org/10.1029/2019gl083301>.
- 559 Wang, R., Lu, Q., Nakamura, R., Huang, C., Du, A., Guo, F., ... Wang, S. (2015). Coalescence
560 of magnetic flux ropes in the ion diffusion region of magnetic reconnection. *Nature Physics*,
561 12(3), 263–267. <https://doi.org/10.1038/nphys3578>.
- 562 Xiao, C. J. (2004). Inferring of flux rope orientation with the minimum variance analysis
563 technique. *Journal of Geophysical Research*, 109(A11).
564 <https://doi.org/10.1029/2004ja010594>.
- 565 Yang, Y. Y., Shen, C., Zhang, Y. C., Rong, Z. J., Li, X., Dunlop, M., ... Rème, H. (2014). The
566 force-free configuration of flux ropes in geomagnetotail: Cluster observations. *Journal of*
567 *Geophysical Research: Space Physics*, 119(8), 6327–6341.
568 <https://doi.org/10.1002/2013ja019642>.
- 569 Zhang, T. L., Baumjohann, W., Teh, W. L., Nakamura, R., Russell, C. T., Luhmann, J. G., ...
570 Balikhin, M. (2012). Giant flux ropes observed in the magnetized ionosphere at Venus.
571 *Geophysical Research Letters*, 39(23). <https://doi.org/10.1029/2012gl054236>.
- 572 Zhang, Y. C., Z. X. Liu, C. Shen, A. Fazakerley, M. Dunlop, H. Rème, E. Lucek, A. P. Walsh,
573 and L. Yao (2007), The magnetic structure of an earthward-moving flux rope observed by
574 Cluster in the near-tail, *Annales Geophysicae*, 25(7), 1471–1476.
- 575 Zhao, C., Russell, C. T., Strangeway, R. J., Petrinec, S. M., Paterson, W. R., Zhou, M., ... Wei,
576 H. Y. (2016). Force balance at the magnetopause determined with MMS: Application to
577 flux transfer events. *Geophysical Research Letters*, 43(23), 11,941–11,947.
578 <https://doi.org/10.1002/2016gl071568>.
- 579 Zhao, J. T., Sun, W. -J., Zong, Q. G., Slavin, J. A., Zhou, X. Z., Dewey, R. M., ... Raines, J. M.
580 (2019). A Statistical Study of the Force Balance and Structure in the Flux Ropes in
581 Mercury's Magnetotail. *Journal of Geophysical Research: Space Physics*, 124(7), 5143–
582 5157. <https://doi.org/10.1029/2018ja026329>.
- 583 Zhao, Y., Wang, R., & Du, A. (2016). Characteristics of field-aligned currents associated with
584 magnetic flux ropes in the magnetotail: A statistical study. *Journal of Geophysical Research:*
585 *Space Physics*, 121(4), 3264–3277. <https://doi.org/10.1002/2015ja022144>.
- 586 Zhou, M., Berchem, J., Walker, R. J., El-Alaoui, M., Deng, X., Cazzola, E., ... Burch, J. L.
587 (2017). Coalescence of Macroscopic Flux Ropes at the Subsolar Magnetopause:

588 Magnetospheric Multiscale Observations. *Physical Review Letters*, 119(5).
589 <https://doi.org/10.1103/physrevlett.119.055101>.
590 Zhou, X.-Z., Zong, Q.-G., Pu, Z. Y., Fritz, T. A., Dunlop, M. W., Shi, Q. Q., ... Wei, Y. (2006).
591 Multiple Triangulation Analysis: another approach to determine the orientation of magnetic
592 flux ropes. *Annales Geophysicae*, 24(6), 1759–1765.
593 <https://doi.org/10.5194/angeo-24-1759-2006>.
594
595
596

Figure1.

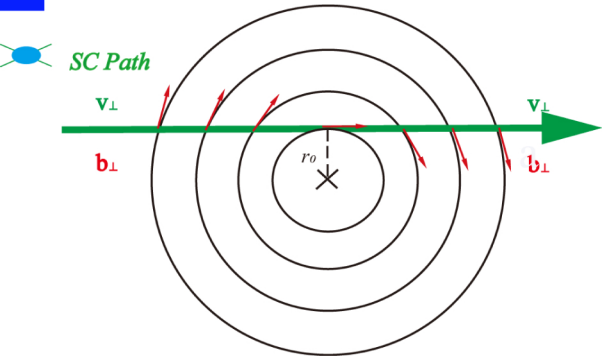
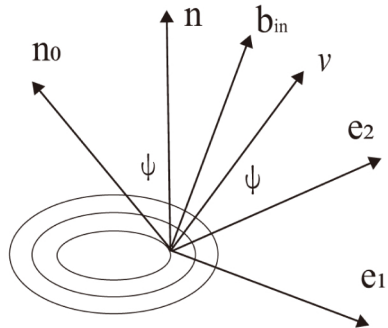
a**b**

Figure2.

2015-10-16 13:04 @MMS3

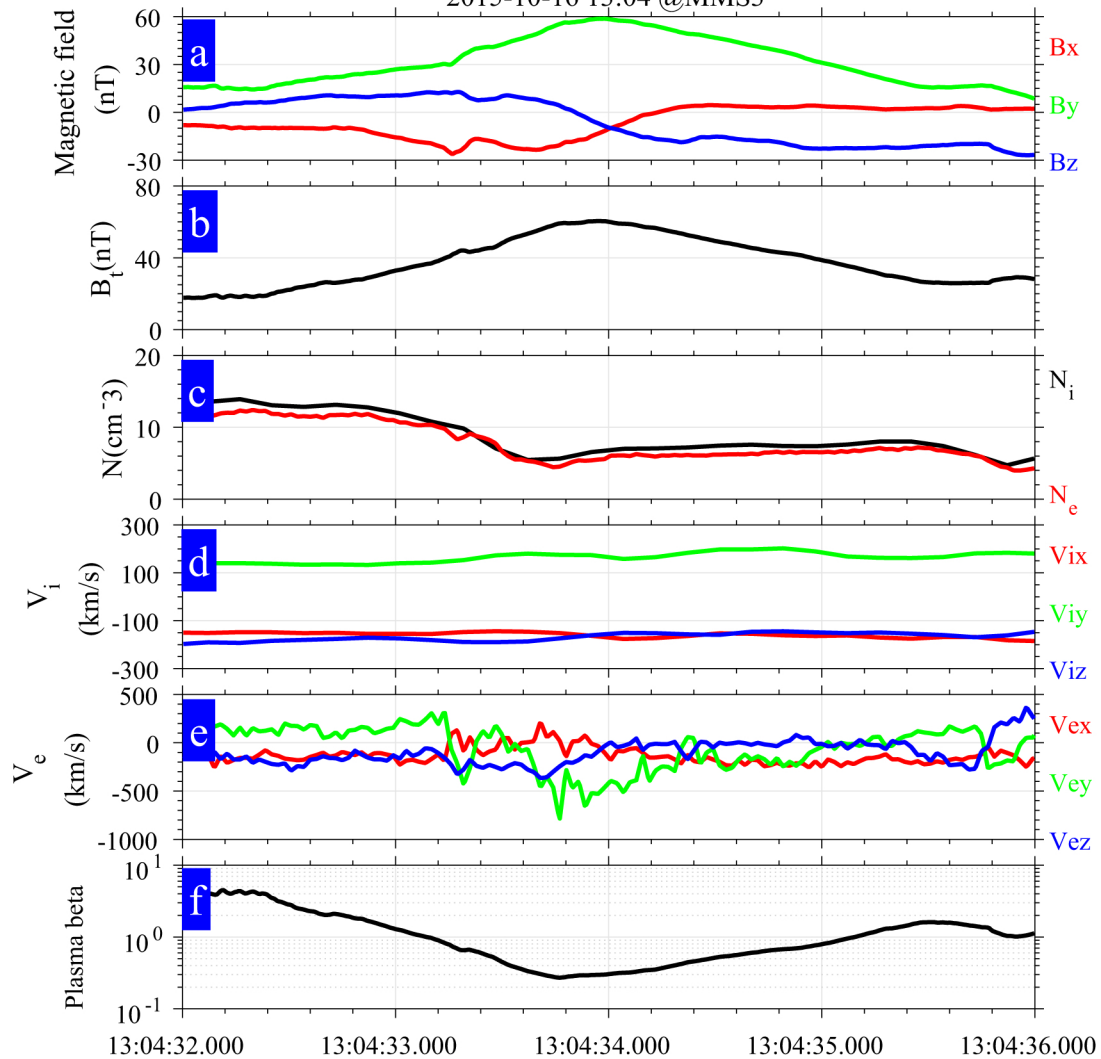


Figure3.

2015-10-16 13:04 @MMS3

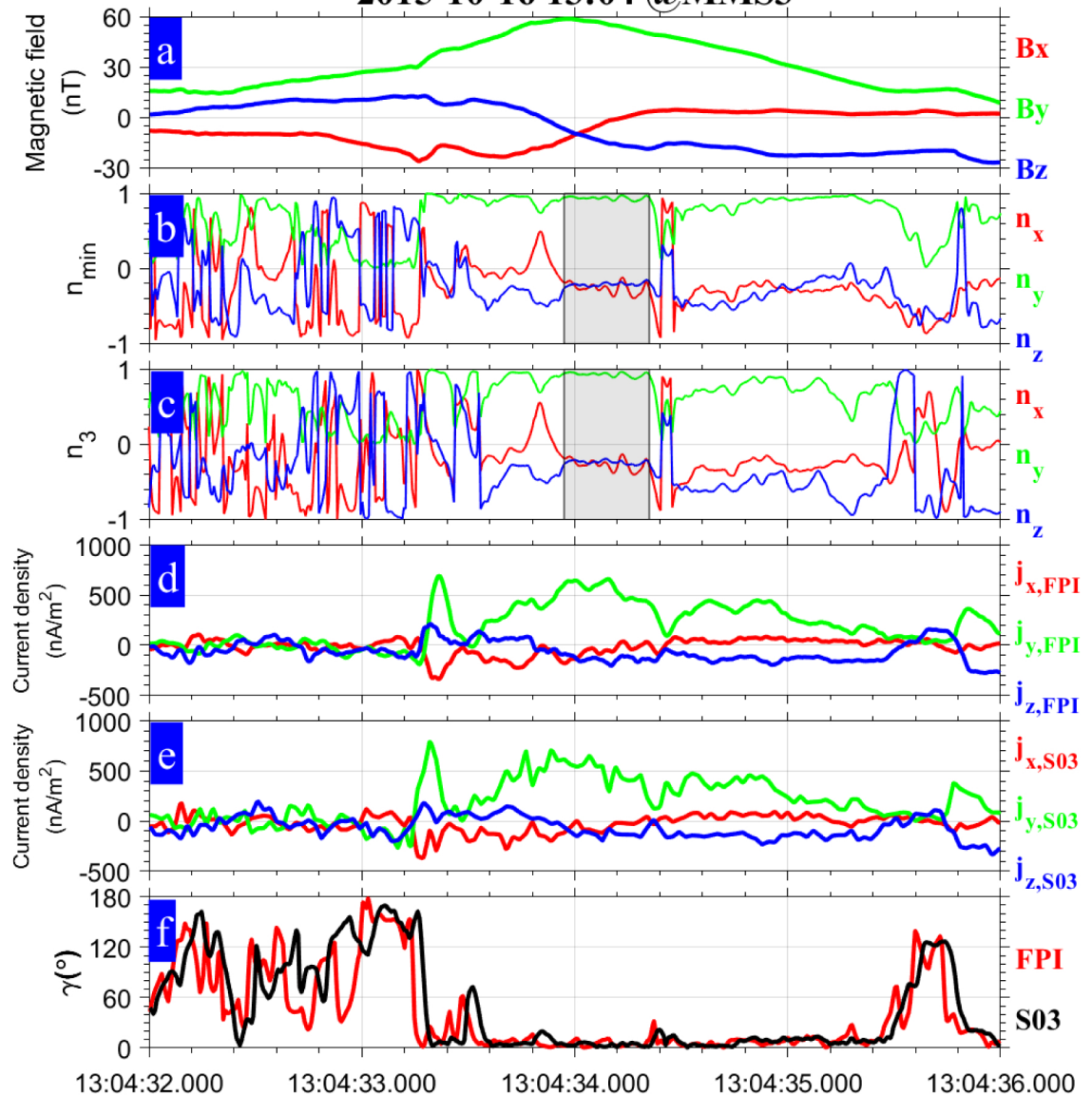


Figure4.

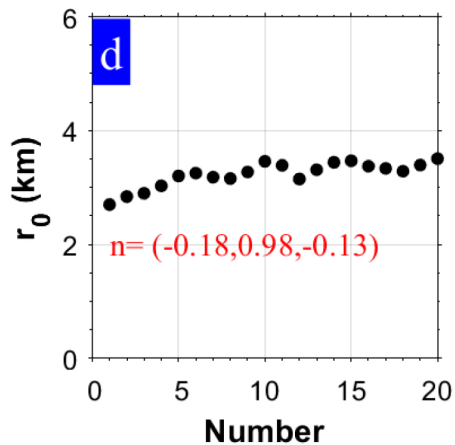
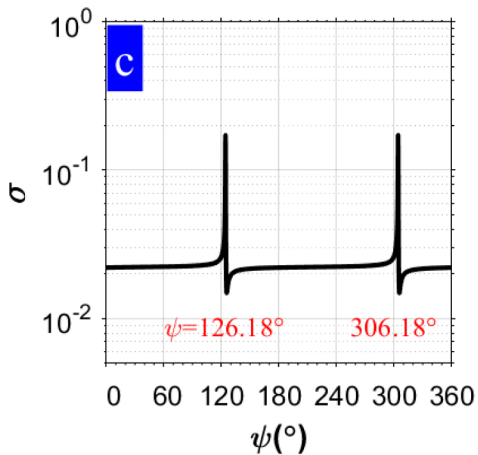
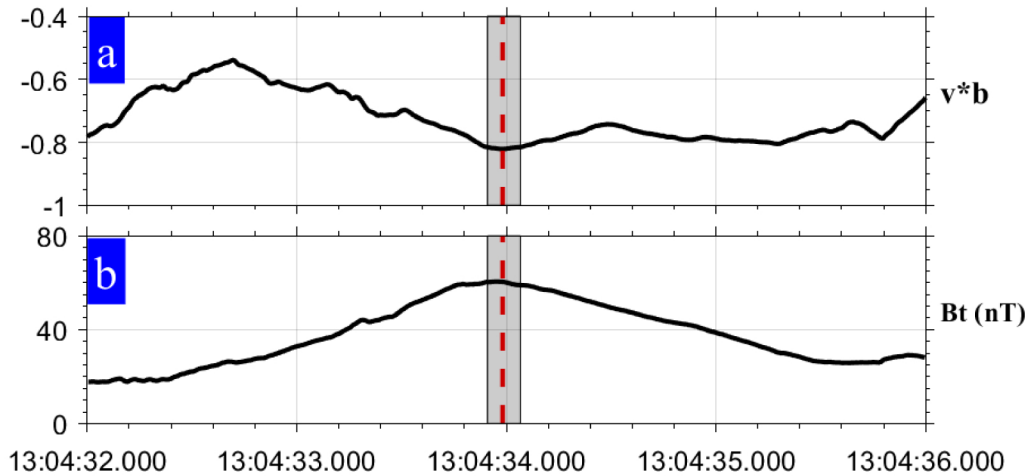


Figure 5.

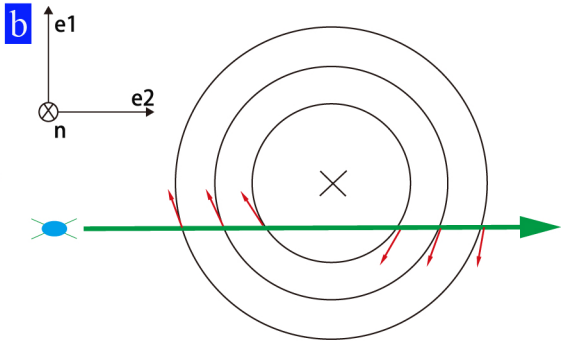
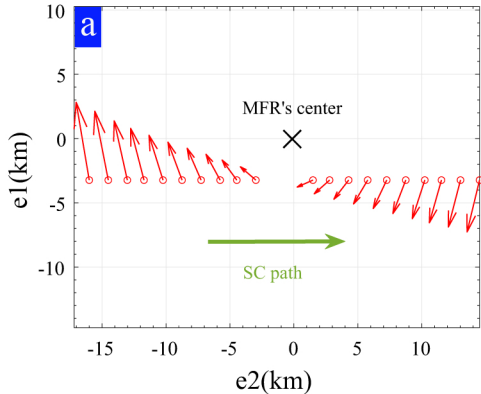
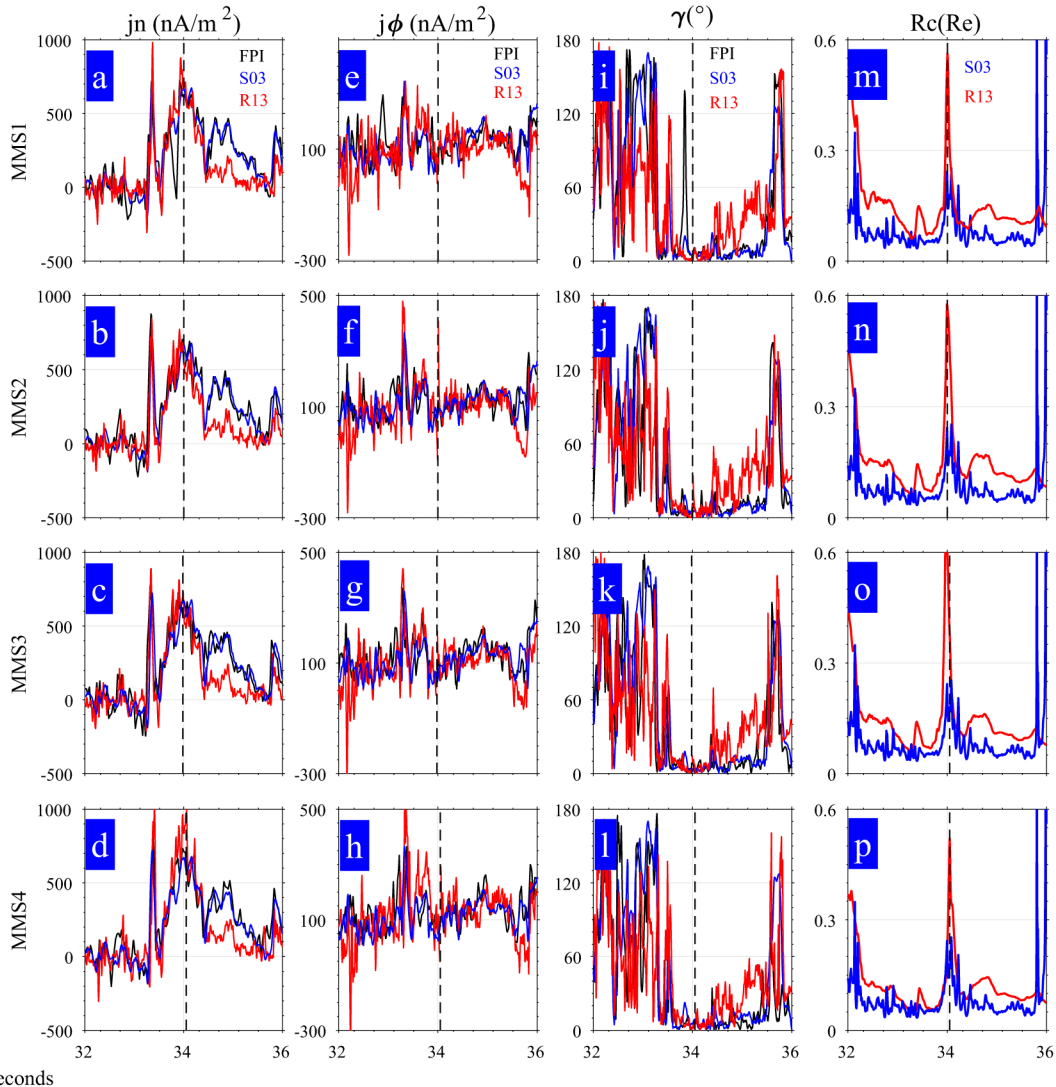


Figure6.



Seconds

Figure7.

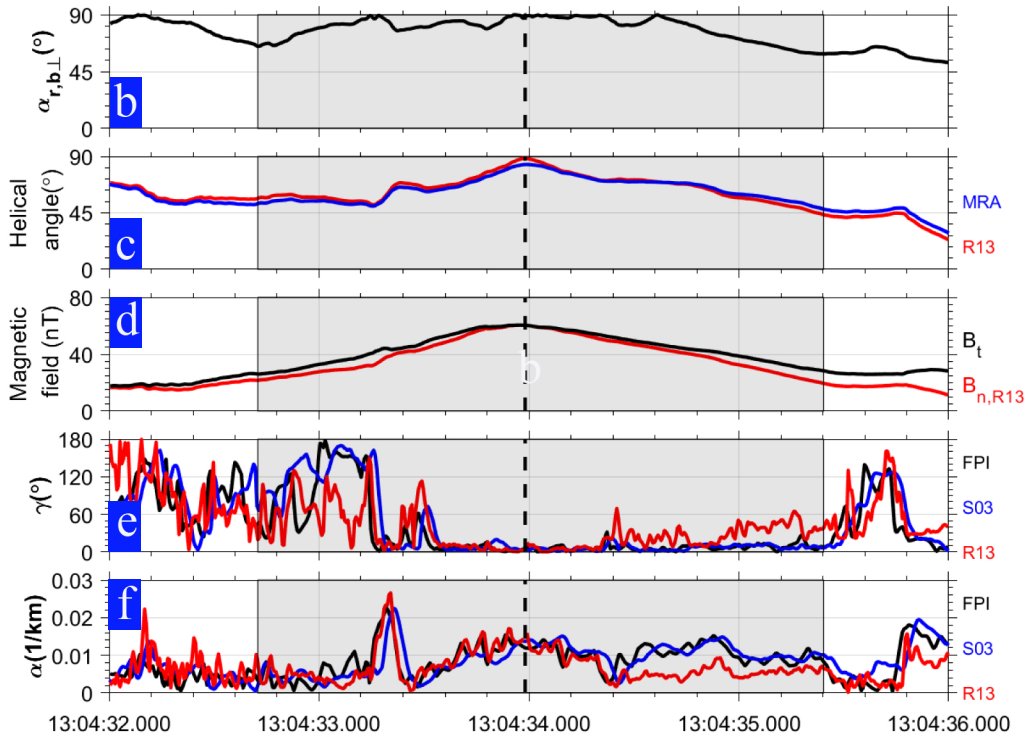
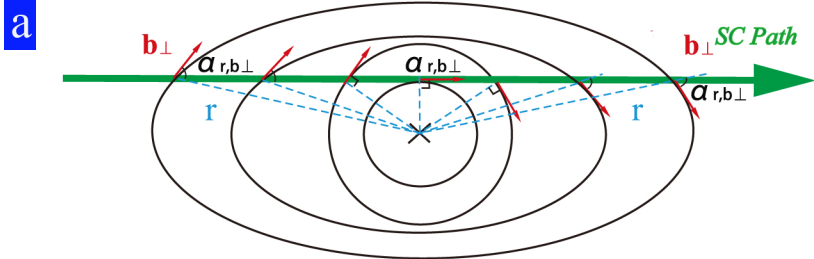


Figure8.

